






# Confined polaronic transport in $(\text{LaFeO}_3)_n/(\text{SrFeO}_3)_1$ superlattices

Cite as: APL Mater. **7**, 071117 (2019); <https://doi.org/10.1063/1.5110190>

Submitted: 14 May 2019 . Accepted: 14 July 2019 . Published Online: 31 July 2019

Seo Hyoung Chang, Seong Keun Kim, Young-Min Kim , Yongqi Dong, Chad M. Folkman, Da Woon Jeong, Woo Seok Choi , Albina Y. Borisevich, Jeffrey A. Eastman , Anand Bhattacharya , and Dillon D. Fong 



View Online



Export Citation



CrossMark

## ARTICLES YOU MAY BE INTERESTED IN

[Self-assembly and properties of domain walls in  \$\text{BiFeO}\_3\$  layers grown via molecular-beam epitaxy](#)

APL Materials **7**, 071101 (2019); <https://doi.org/10.1063/1.5103244>

[Valence band offsets for ALD  \$\text{SiO}\_2\$  and  \$\text{Al}\_2\text{O}\_3\$  on  \$\(\text{In}\_x\text{Ga}\_{1-x}\)\_2\text{O}\_3\$  for  \$x = 0.25-0.74\$](#)

APL Materials **7**, 071115 (2019); <https://doi.org/10.1063/1.5110498>

[Determining interface structures in vertically aligned nanocomposite films](#)

APL Materials **7**, 061105 (2019); <https://doi.org/10.1063/1.5099204>

additive manufacturing    epitaxial crystal growth    cerium oxide polishing powder    silver nanoparticles    sputtering targets

deposition slugs    OLED Lighting    spintronics    solar energy

GDC    Li-ion battery electrolytes    99.999% ruthenium spheres

endoheedral fullerenes    copper nanoparticles    diamond micropowder

CIGS    MBE grade materials    palladium catalysts    flexible electronics

beta-barium borate    borosilicate glass    dysprosium pellets    YBCO

pyrolytic graphite    3d graphene foam    indium tin oxide    mesoporus silica

raman substrates    sapphire windows    tungsten carbide    InGaAs

barium fluoride    carbon nanotubes    lithium niobate    scandium powder

III-IV semiconductors    CVD precursors    europium phosphors

InAs wafers    laser crystals    ultra high purity materials    MOFs

rare earth metals    photovoltaics    refractory metals    MOCVD

superconductors    transparent ceramics    ultra high purity silicon

**American Elements**  
THE ADVANCED MATERIALS MANUFACTURER®

**Now Invent.**  
The Next Generation of Material Science Catalogs

perovskite crystals    yttrium iron garnet    alternative energy    h-BN

gold nanocubes    graphene oxide    macromolecules    photonics

rhodium sponge    fiber optics    beamsplitters    infrared dyes    zeolites

fused quartz    metallocenes    platinum ink    buckyballs    Ti-6Al-4V

American Elements opens up a world of possibilities so you can **Now Invent!**

Over 15,000 certified high purity laboratory chemicals, metals, & advanced materials and a state-of-the-art Research Center. Printable GHS-compliant Safety Data Sheets. Thousands of new products. And much more. All on a secure multi-language 'Mobile Responsive' platform.

[www.americanelements.com](http://www.americanelements.com)



# Confined polaronic transport in $(\text{LaFeO}_3)_n/(\text{SrFeO}_3)_1$ superlattices

Cite as: APL Mater. 7, 071117 (2019); doi: 10.1063/1.5110190

Submitted: 14 May 2019 • Accepted: 14 July 2019 •

Published Online: 31 July 2019



Seo Hyung Chang,<sup>1,2,a)</sup> Seong Keun Kim,<sup>1,3,a)</sup> Young-Min Kim,<sup>4,5</sup> Yongqi Dong,<sup>1,6</sup> Chad M. Folkman,<sup>1</sup> Da Woon Jeong,<sup>7</sup> Woo Seok Choi,<sup>8</sup> Albina Y. Borisevich,<sup>4</sup> Jeffrey A. Eastman,<sup>1</sup> Anand Bhattacharya,<sup>1</sup> and Dillon D. Fong<sup>1,b)</sup>

## AFFILIATIONS

<sup>1</sup>Materials Science Division, Argonne National Laboratory, Argonne, Illinois 60439, USA

<sup>2</sup>Department of Physics, Chung-Ang University, Seoul 06974, South Korea

<sup>3</sup>Center for Electronic Materials, Korea Institute of Science and Technology, Seoul 02792, South Korea

<sup>4</sup>Materials Science and Technology Division, Oak Ridge National Laboratory, Oak Ridge, Tennessee 37831, USA

<sup>5</sup>Department of Energy Science, Sungkyunkwan University, Suwon 16419, South Korea

<sup>6</sup>National Synchrotron Radiation Laboratory, University of Science and Technology of China, Hefei, Anhui 230026, China

<sup>7</sup>Department of Physics and Astronomy, Seoul National University, Seoul 08826, South Korea

<sup>8</sup>Department of Physics, Sungkyunkwan University, Suwon 16419, South Korea

<sup>a)</sup>Contributions: S. H. Chang and S. K. Kim contributed equally to this work.

<sup>b)</sup>Electronic mail: [fong@anl.gov](mailto:fong@anl.gov)

## ABSTRACT

Functional oxide superlattices offer new and exciting possibilities for the exploration of emergent properties at the nanoscale. While the behavior of  $\text{La}_{1-x}\text{Sr}_x\text{FeO}_3$  films has been extensively investigated at low temperatures, few studies have been carried out at high temperatures, particularly for  $\text{LaFeO}_3/\text{SrFeO}_3$  superlattice systems. Here, we investigate the transport behavior and optical properties of  $(\text{LaFeO}_3)_n/(\text{SrFeO}_3)_1$  superlattices at 373 K and above. Using optical spectroscopy, we observe a low energy excitation at  $\sim 1$  eV, attributable to charge transfer between the O  $2p$  and Fe  $3d$  states of the  $\delta$ -doped single  $\text{SrFeO}_3$  layer. From in-plane conductivity measurements on the superlattices, we determine activation energies that are much lower than those of alloyed samples and vary with the total number of  $\text{SrFeO}_3$  layers. This suggests that polaronic transport is confined near the  $\text{SrFeO}_3$  regions, permitting mobilities significantly enhanced over those in alloyed thin films.

© 2019 Author(s). All article content, except where otherwise noted, is licensed under a Creative Commons Attribution (CC BY) license (<http://creativecommons.org/licenses/by/4.0/>). <https://doi.org/10.1063/1.5110190>

$\text{La}_{1-x}\text{Sr}_x\text{FeO}_3$  (LSFO) is a strongly correlated oxide known to display a variety of unique material properties. While it exhibits many interesting electronic and magnetic transitions near or below room temperature,<sup>1–3</sup> at higher temperatures its mixed ionic-electronic properties make it useful for sensors, catalysts, solid oxide fuel cells, and a host of other energy-related applications.<sup>4–11</sup> Researchers can now directly examine the fundamental mechanisms governing transport at these elevated temperatures, utilizing model systems and state-of-the-art characterization probes to help distinguish between the effects of microstructure and intrinsic/extrinsic contributors to electrical conduction.<sup>12–15</sup> Here we exploit advances

in oxide thin film synthesis to investigate the properties of modulation doped (001)-oriented epitaxial heterostructures with SrO layers periodically inserted into the  $\text{LaFeO}_3$  matrix. Such atomically controlled, layered structures allow the study of cation ordering effects on electronic behavior,<sup>16–19</sup> a topic of increasing interest in materials design<sup>20–22</sup> and the one that may lead to the development of novel materials for energy.<sup>23,24</sup>

The substitution of  $\text{Sr}^{2+}$  for  $\text{La}^{3+}$  in the charge-transfer insulator  $\text{LaFeO}_3$  leads to increased  $p$ -type conductivity up to  $x = 0.5$ . Electronic transport is known to occur by small polaron conduction,<sup>25</sup> involving thermally activated hops of hole polarons between

states of primarily oxygen character, as the Fe ions have been found to remain in the  $3d^5$  configuration up to  $x \approx 0.5$ .<sup>26</sup> At the limit of  $x = 1$ , perovskite  $\text{SrFeO}_3$  is a well-known metal,<sup>27,28</sup> and the conductivity of LSFO increases with higher Sr concentration. Previous transport studies, however, did not address the effect of geometric confinement in the LSFO films.

Here, we focus on *p*-type electronic transport in (001)-oriented  $(\text{LaFeO}_3)_n/(\text{SrFeO}_3)_1$  or  $(\text{LFO})_n/(\text{SFO})$  superlattices at elevated temperatures (373–673 K) and high oxygen pressures (1300 Pa), where a supercell consists of  $n$  consecutive layers of  $\text{LaFeO}_3$  and a single layer of  $\text{SrFeO}_3$ . The superlattices were grown by ozone-assisted molecular beam epitaxy (MBE) on  $\text{TiO}_2$ -terminated  $\text{SrTiO}_3$  (001) substrates.<sup>29</sup> Throughout deposition, the ozone pressure in the chamber was fixed at  $2.7 \times 10^{-4}$  Pa and the sample temperature kept at 923 K. Fluxes from the La, Sr, and Fe effusion cells were calibrated prior to growth. For deposition of the artificially ordered layers, we employed the sequential deposition method, alternately opening and closing each cation species for a time calibrated to result in the deposition of one monolayer. *In situ* reflection high-energy electron diffraction (RHEED) was used to monitor the growth process, and we observed pronounced intensity oscillations of the specular reflection throughout deposition. Superlattices with  $n = 1, 2, 4, 7, \text{ and } 16$  were grown, always starting and terminating with a  $\text{LaFeO}_3$  layer, leading to approximate Sr concentrations of  $x = 0.50, 0.33, 0.20, 0.125, \text{ and } 0.059$ , respectively. A pure  $\text{LaFeO}_3$  film and a random alloy of  $\text{La}_{0.875}\text{Sr}_{0.125}\text{FeO}_3$  grown by codeposition of La and Sr were used for reference. The total film thickness,  $t$ , was kept between 32 and 35 unit cells.

The structure of the superlattices was studied with x-ray reflectivity (XRR) using  $\text{Cu } K_\alpha$  radiation (Bruker D8 Discover), atomic force microscopy (AFM, Asylum Research MFP-3D), and cross-sectional scanning transmission electron microscopy (STEM) using a NION UltraSTEM100 operated at 100 kV. Since LSFO is a known

mixed conductor, we performed both in-plane direct and alternating current (DC and AC) electrical measurements using a Keithley 2400 Sourcemeter and a CH Instruments 760D potentiostat, respectively. The electrical measurements were conducted in an environmental probe station capable of a wide variety of temperatures (300–1200 K) and gas environments. Optical properties of superlattices were measured by spectroscopic ellipsometry (VASE Ellipsometer, J. A. Woollam Co., Inc.) at room temperature. Since the optical wavelengths were much longer than the superlattice periodicities, each sample was approximated as a single effective medium for analysis.<sup>30</sup>

A representative AFM image of the  $(\text{LFO})_n/(\text{SFO})$  surface after growth is shown in Fig. 1(a). As seen, the  $\sim 0.4$  nm step height from the  $\text{SrTiO}_3$  substrate was preserved during the growth process. This, along with the observed RHEED oscillations during growth, indicates that the superlattices were grown in a layer-by-layer fashion, resulting in atomically smooth surfaces and little to no excess material. The XRR data shown in Fig. 1(b) indicate that the superlattice structures were maintained after growth at high temperature, with interfacial roughnesses ranging from 0.1 to 0.3 nm, replicating the surface roughness of the substrate. Evidence for sharp interfaces can also be seen in the cross-sectional high-angle annular dark-field (HAADF) STEM image for one of the superlattice systems,  $(\text{LFO})_2/(\text{SFO})$ , as shown in Fig. 1(c). Long-range periodicity is observed along the growth direction, consisting of two bright layers alternating with one dark layer, due to the higher atomic number of La compared with Sr. Chemical mapping with electron energy-loss spectroscopy (EELS) [Fig. 1(d)] shows that the cation distribution in the superlattice follows the intended ordering sequence, with little to no La signal in the darker layers and uniform Fe distribution.

The average out-of-plane lattice constant,  $c$ , as measured from high x-ray angle diffraction (Fig. S1) decreases from 0.393(1) nm to

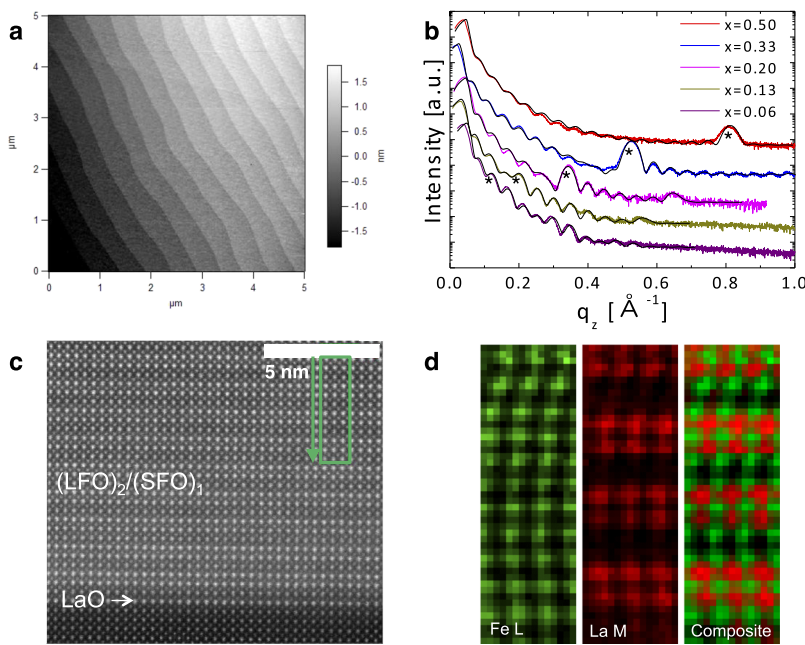


**FIG. 1.** Structural results of the  $(\text{LFO})_n/(\text{SFO})$  superlattices. (a) Representative AFM image of the film surface [from the  $(\text{LFO})_4/(\text{SFO})$  superlattice]. (b) Low-angle X-ray reflectivity measurements from the  $(\text{LFO})_n/(\text{SFO})$  superlattices. The first order superlattice X-ray reflections are indicated by the asterisks. (c) Cross-sectional HAADF STEM image of the  $(\text{LFO})_2/(\text{SFO})$  superlattice film grown on  $\text{TiO}_2$ -terminated  $\text{SrTiO}_3$  (001). As depicted, the first deposited layer is LaO. The alternating bright and dark layers stem from the different atomic numbers of La and Sr. (d) Chemical maps obtained from the EELS spectra for the area marked with a green rectangle in (c) showing Fe (green; integrated Fe  $L_{2,3}$  edge intensity) and La (red; integrated La  $M_{4,5}$ ) atomic column distributions. The composite image was obtained from the two maps after intensity normalization. Note that vertical distortions in the maps are artifacts due to specimen drift during the acquisition.

0.388(1) nm as  $x$  increases from 0.059 to 0.5, respectively. These values are in good agreement with the pseudocubic lattice parameters of air-cooled, bulk LSFO,<sup>8,31</sup> as well as fully-oxidized epitaxial thin films.<sup>15,32</sup> The  $c$  vs  $x$  behavior is as expected based on the small misfit strain with respect to the substrate, which ranges from  $-0.6\%$  to  $+0.5\%$  as  $x$  is varied from 0 to 0.5.

Figure 2(a) shows 300 K data for the real part of the optical conductivity spectra,  $\sigma_1(\omega)$ . The transition at  $\sim 3.2$  eV for pure LaFeO<sub>3</sub> stems from the electronic band gap. Using well-established procedures,<sup>33</sup> we determine an optical bandgap of 2.68(2) eV for LaFeO<sub>3</sub>, which is in good agreement with the prior result of 2.64 eV from Scafetta *et al.*<sup>15</sup> Similar to the results for alloyed LSFO films,<sup>15,34</sup> Sr doping induces a red shift in this transition. We also observe the appearance of a transition at  $\sim 1.2$  eV, attributed to states formed within the bandgap and from which we can extract a new, smaller bandgap as a function of Sr concentration [Fig. 2(a), inset].

With an increasing amount of Sr, we observe the following systematic changes in the electronic structure of the superlattices:

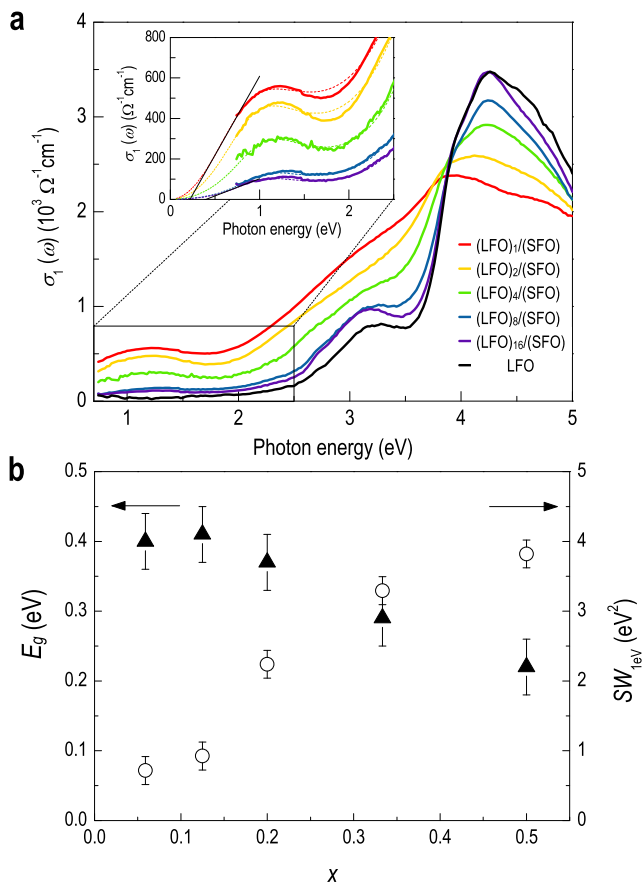


**FIG. 2.** Results of room temperature optical measurements on (LFO)<sub>*n*</sub>/(SFO) superlattices. (a) The real part of the optical conductivity,  $\sigma_1(\omega)$ , for the superlattices. The inset shows  $\sigma_1(\omega)$  at the low photon energy region near 1 eV. (b) The dependence of bandgap ( $E_g$ ) and the spectral weight ( $SW$  at 1 eV) on the Sr doping ratio,  $x$ .

(1) the appearance and development of absorption in the midgap region at  $\sim 1$  eV; (2) increasing spectral weight (SW) at the  $\sim 3$  eV photon energy range; (3) decreasing spectral weight above 4 eV. The prominent amount of absorption at around 1 eV and 2–3 eV can be attributed to charge transfer transitions between O 2*p* and various Fe 3*d* orbital states (O 2*p* to Fe 3*d*  $t_{2g}$  and  $e_g$ , respectively).<sup>15,35–39</sup>

The nature of the  $\sim 1$  eV peak is the key to understanding transport properties of the ferrite system. To obtain further insights into this low energy excitation, we plot the bandgap of the absorption and its spectral weight [ $SW = \int \sigma_1(\omega) d\omega$ ] as a function of Sr doping ( $x$ ), as shown in Fig. 2(b). Due to the wavelength limitation of the spectroscopic ellipsometer (1,700 nm), we also measured the reflectance spectra of the superlattices down to the mid-infrared range (0.07 eV) and confirmed the low-photon-energy tail based on the fitting of reflectance spectra, shown as dotted lines in the inset of Fig. 2(a). As seen, the SW of the  $\sim 1$  eV absorption peak almost increases linearly with  $x$ , possibly due to the increased hole concentration with Sr doping within the superlattice. Therefore, the peak can be attributed to the newly introduced electronic states from the SrFeO<sub>3</sub> layers in the superlattice.<sup>39</sup> The optical bandgap determined at lower absorption energies also shows a systematic trend. Interestingly, these values are consistent with the activation energies obtained from the previous high temperature transport measurements on alloyed LSFO samples.<sup>32</sup>

To address the effect of geometric confinement within the (LFO)<sub>*n*</sub>/(SFO) superlattices on the transport properties, electrical measurements were performed using platinum interdigitated electrodes with 5  $\mu\text{m}$  spacing. AC measurements performed between  $10^{-1}$  Hz and  $10^5$  Hz showed no evidence of frequency dispersion up to 673 K resulting in conductance values nearly identical to those from the DC experiments, suggesting that ionic transport is not a major contributor to the electrical conductivity in this temperature range. Consequently, all of the values reported here were obtained from DC measurements conducted after an initial 60 min oxygen anneal at a fixed oxygen partial pressure of 1300 Pa, with a maximum temperature of 673 K to minimize the degree of interdiffusion.<sup>40</sup> The samples were given at least 2 h to equilibrate after changing temperatures and reach time-independent conductance values. Room temperature XRR measurements taken from a sample before and after annealing at both 473 K and 673 K are shown in Fig. S2 of the [supplementary material](#). As seen, anneals at these temperatures had a negligible effect on the cation-ordered structure.

For the small, nonadiabatic polaron hopping mechanism, the conductivity is predicted to have the following temperature dependence:<sup>41,42</sup>

$$\sigma = \frac{\sigma_0}{T^{3/2}} e^{-E_a/k_B T} \quad (1)$$

where  $\sigma_0$  is a pre-exponential factor,  $E_a$  is the activation energy, and  $k_B$  is the Boltzmann constant. A plot of  $\sigma T^{3/2}$  vs  $1000/T$  is shown in Fig. 3(a) for both the cation-ordered superlattices and the random alloy film. The conductivities follow the Arrhenius behavior predicted in Eq. (1), in accordance with the small polaron model, and increase with the Sr concentration,  $x$ , as expected based on carrier doping. Interestingly, all of the superlattices exhibit higher

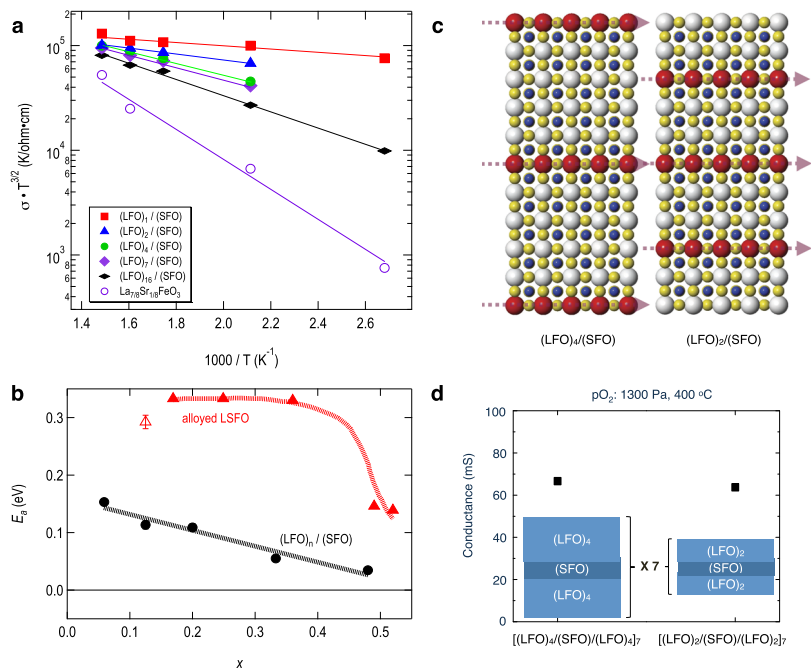


**FIG. 3.** Results of electrical measurements on the  $(\text{LFO})_n/(\text{SFO})$  superlattices at a fixed oxygen partial pressure of 1300 Pa. (a) The product of conductivity and temperature to the 3/2 power as a function of inverse temperature. The filled symbols are for the superlattices, while the open circles are for the alloyed LSFO film. The error bars are within the size of the symbols. (b) The determined activation energies for hole transport (black circles) as a function of  $x$  or, equivalently, the inverse bilayer spacing. The error bars are within the size of the symbols. The red triangles are the measured activation energies for alloyed films from Xie *et al.*<sup>32</sup> The result from the  $x = 0.125$  sample is shown as the open triangle. (c) Schematics illustrating in-plane polaronic hopping along the SFO layers (where the red spheres represent Sr cations). (d) Conductance data for  $(\text{LFO})_8/(\text{SFO})$  (63 unit cells) and  $(\text{LFO})_4/(\text{SFO})$  (35 unit cells) superlattice samples.

conductivities than that of the  $x = 0.125$  random alloy (open violet circles), even for samples with lower Sr concentration. The activation energies determined from the fitted Arrhenius relationships in Fig. 3(a) are shown in (b) (black circles). Results from random alloy LSFO films<sup>32</sup> are also provided (red triangles). There is a decrease in activation energy with increasing Sr concentration for all samples. For alloyed LSFO samples, this has been attributed to the increased probability of hopping between the energy states of neighboring polarons.<sup>43</sup>

As seen in Fig. 3, the cation-ordered structures exhibit activation energies smaller than those for the random alloy samples, by roughly 0.2 eV (except at  $x = 0.5$ ). Since the hole concentrations of the superlattice samples in Fig. 2(b) scale with the degree of Sr doping, it appears that the reduced activation energy of the superlattices originates from an enhancement in mobility related to cation ordering. The decrease in activation energy with  $x$  also indicates that hole transport is not perturbed by cation disorder and may be confined to the  $\text{SrFeO}_3$  layers, as shown in Fig. 3(c). If increasing  $x$  implies a progression toward more metallic perovskite  $\text{SrFeO}_3$  rather than more insulating brownmillerite  $\text{SrFeO}_{2.5}$ , one can reasonably explain the decrease in bandgap and the increase in conductivity in the superlattices. In fact, the  $\sim 1$  eV low energy absorption peak in Fig. 2(b) is a signature of the perovskite  $\text{SrFeO}_3$  structure.<sup>39</sup>

To confirm confined, in-plane polaronic hopping along the  $\text{SrFeO}_3$  layers, we fabricated  $(\text{LFO})_8/(\text{SFO})$  and  $(\text{LFO})_4/(\text{SFO})$  superlattices, each with a total of seven SFO layers (63 and 35 unit cells thick, respectively). The conductance of  $(\text{LFO})_8/(\text{SFO})$  is nearly the same as that of the  $(\text{LFO})_4/(\text{SFO})$  superlattice, as shown in Fig. 3(d). The conductance therefore appears to be independent of both the total thickness and the number of  $\text{LaFeO}_3$  unit cells. This shows that the change in conductance is mainly dependent on

the number of  $\text{SrFeO}_3$  layers and not the LFO:SFO ratio, which is markedly different from the behavior of alloyed LSFO samples. This discrepancy between the alloy samples and our superlattices can be understood if the polarons are geometrically confined to the  $\text{SrFeO}_3$  layers. Note that both the formation energy of oxygen vacancies in  $\text{SrFeO}_3$  (about 0.4 eV) and the energy for ionic conduction in bulk  $\text{SrFeO}_3$  (about 0.5 eV) are larger than the activation energies observed here.<sup>44,45</sup>

In summary, we report the observation of confined transport behavior in  $(\text{LFO})_n/(\text{SFO})$  superlattices at high temperatures. The results of optical spectroscopy indicate enhanced absorption at around 1 eV, originating from charge transfer between the O 2p and Fe 3d  $t_{2g}$  states. Changes in the corresponding bandgap are consistent with changes in the activation energies of the  $(\text{LFO})_n/(\text{SFO})$  superlattices as a function of the Sr concentration. The lower activation energies of  $(\text{LFO})_n/(\text{SFO})$  superlattices as compared to those of alloyed LSFO samples may be understood in terms of confined polaronic transport. While spectroscopic measurements of the high temperature electronic structure would be worthwhile, this initial study provides important insights into unique properties of digitally synthesized materials.

See [supplementary material](#) for high angle,  $\theta - 2\theta$  x-ray diffraction scans (using Cu  $K\alpha$  radiation) from all of the superlattices and low angle reflectivity scans from one of the superlattices, illustrating the effect of annealing on superlattice structures.

Work by S. K. Kim, Y.-M. Kim, Y. Dong, C. M. Folkman, D. W. Jeong, A. Y. Borisevich, J. A. Eastman, A. Bhattacharya, and D. D. Fong was supported by the U.S. Department of Energy (DOE), Office of Science, Basic Energy Sciences (BES), Materials Sciences and Engineering Division. Work by S. H. Chang was supported by the Chung-Ang University Research Grants in 2017.

## REFERENCES

- <sup>1</sup>J. B. Goodenough and J. S. Zhou, *Localized to Itinerant Electronic Transition in Perovskite Oxides* (Springer, 2001), Vol. 98, p. 17.
- <sup>2</sup>H. Wadati, D. Kobayashi, A. Chikamatsu, R. Hashimoto, M. Takizawa, K. Horiba, H. Kumigashira, T. Mizokawa, A. Fujimori, M. Oshima, M. Lippmaa, M. Kawasaki, and H. Koinuma, *J. Electron Spectrosc. Relat. Phenom.* **144-147**, 877 (2005).
- <sup>3</sup>H. Wadati, A. Chikamatsu, M. Takizawa, R. Hashimoto, H. Kumigashira, T. Yoshida, T. Mizokawa, A. Fujimori, M. Oshima, M. Lippmaa, M. Kawasaki, and H. Koinuma, *Phys. Rev. B* **74**, 115114 (2006).
- <sup>4</sup>J. Mizusaki, M. Yoshihiro, S. Yamauchi, and K. Fueki, *J. Solid State Chem.* **58**, 257 (1985).
- <sup>5</sup>E. V. Bongio, H. Black, F. C. Raszewski, D. Edwards, C. J. McConville, and V. R. Amarakoon, *J. Electroceram.* **14**, 193 (2005).
- <sup>6</sup>E. Bucher and W. Sitte, *Solid State Ionics* **173**, 23 (2004).
- <sup>7</sup>M. V. Patrakeev, I. A. Leonidov, V. L. Kozhevnikov, and K. R. Poeppelmeier, *J. Solid State Chem.* **178**, 921 (2005).
- <sup>8</sup>M. V. Patrakeev, J. A. Bahteeva, E. B. Mitberg, I. A. Leonidov, V. L. Kozhevnikov, and K. R. Poeppelmeier, *J. Solid State Chem.* **172**, 219 (2003).
- <sup>9</sup>J. Bahteeva, I. Leonidov, M. Patrakeev, E. Mitberg, V. Kozhevnikov, and K. Poeppelmeier, *J. Solid State Electrochem.* **8**, 578 (2004).
- <sup>10</sup>M. Søgaard, P. Vang Hendriksen, and M. Mogensen, *J. Solid State Chem.* **180**, 1489 (2007).
- <sup>11</sup>I. Waernhus, T. Grande, and K. Wiik, *Top. Catal.* **54**, 1009 (2011).
- <sup>12</sup>A. Braun, J. Richter, A. S. Harvey, S. Erat, A. Infortuna, A. Frei, E. Pomjakushina, B. S. Mun, P. Holtappels, U. Vogt, K. Conder, L. J. Gauckler, and T. Graule, *Appl. Phys. Lett.* **93**, 262103 (2008).
- <sup>13</sup>A. Braun, X. Zhang, Y. Sun, U. Müller, Z. Liu, S. Erat, M. Ari, H. Grimmer, S. S. Mao, and T. Graule, *Appl. Phys. Lett.* **95**, 022107 (2009).
- <sup>14</sup>A. Braun, S. Erat, A. K. Ariffin, R. Mancke, H. Wadati, T. Graule, and L. J. Gauckler, *Appl. Phys. Lett.* **99**, 202112 (2011).
- <sup>15</sup>M. D. Scafetta, Y. J. Xie, M. Torres, J. E. Spanier, and S. J. May, *Appl. Phys. Lett.* **102**, 081904 (2013).
- <sup>16</sup>A. Ohtomo, D. A. Muller, J. L. Grazul, and H. Y. Hwang, *Nature* **419**, 378 (2002).
- <sup>17</sup>A. Bhattacharya, X. Zhai, M. Warusawithana, J. N. Eckstein, and S. D. Bader, *Appl. Phys. Lett.* **90**, 222503 (2007).
- <sup>18</sup>S. J. May, P. J. Ryan, J. L. Robertson, J. W. Kim, T. S. Santos, E. Karapetrova, J. L. Zarestky, X. Zhai, S. G. E. te Velthuis, J. N. Eckstein, S. D. Bader, and A. Bhattacharya, *Nat. Mater.* **8**, 892 (2009).
- <sup>19</sup>D. G. Ouellette, P. Moetakef, T. A. Cain, J. Y. Zhang, S. Stemmer, D. Emin, and S. J. Allen, *Sci. Rep.* **3**, 3284 (2013).
- <sup>20</sup>S. M. Nakhmanson and I. Naumov, *Phys. Rev. Lett.* **104**, 097601 (2010).
- <sup>21</sup>J. M. Rondinelli and N. A. Spaldin, *Adv. Mater.* **23**, 3363 (2011).
- <sup>22</sup>J. M. Rondinelli and C. J. Fennie, *Adv. Mater.* **24**, 1961 (2012).
- <sup>23</sup>A. Tarancón, M. Burriel, J. Santiso, S. J. Skinner, and J. A. Kilner, *J. Mater. Chem.* **20**, 3799 (2010).
- <sup>24</sup>J. Ravichandran, A. K. Yadav, R. Cheaito, P. B. Rossen, A. Soukiassian, S. J. Suresha, J. C. Duda, B. M. Foley, C.-H. Lee, Y. Zhu, A. W. Lichtenberger, J. E. Moore, D. A. Muller, D. G. Schlom, P. E. Hopkins, A. Majumdar, R. Ramesh, and M. A. Zurbuchen, *Nat. Mater.* **13**, 168 (2013).
- <sup>25</sup>W.-H. Jung, *Physica B* **299**, 120 (2001).
- <sup>26</sup>M. Abbate, F. De Groot, J. C. Fuggle, A. Fujimori, O. Strebel, F. Lopez, M. Domke, G. Kaindl, G. A. Sawatzky, and M. Takano, *Phys. Rev. B* **46**, 4511 (1992).
- <sup>27</sup>P. Adler, A. Lebon, V. Damjanović, C. Ulrich, C. Bernhard, A. V. Boris, A. Maljuk, C. T. Lin, and B. Keimer, *Phys. Rev. B* **73**, 094451 (2006).
- <sup>28</sup>S. Ishiwata, M. Tokunaga, Y. Kaneko, D. Okuyama, Y. Tokunaga, S. Wakimoto, K. Kakurai, T. Arima, Y. Taguchi, and Y. Tokura, *Phys. Rev. B* **84**, 054427 (2011).
- <sup>29</sup>G. Koster, B. L. Kropman, G. J. Rijnders, D. H. Blank, and H. Rogalla, *Appl. Phys. Lett.* **73**, 2920 (1998).
- <sup>30</sup>D. W. Jeong, W. S. Choi, T. D. Kang, C. H. Sohn, A. David, H. Rotella, A. A. Sirenko, C. H. Lee, J. H. Kim, U. Lüders, W. Prellier, Y. J. Kim, Y. S. Lee, and T. W. Noh, *Phys. Rev. B* **84**, 115132 (2011).
- <sup>31</sup>A. Fossdal, M. Menon, I. Waernhus, K. Wiik, M.-A. Einarsrud, and T. Grande, *J. Am. Ceram. Soc.* **87**, 1952 (2004).
- <sup>32</sup>Y. J. Xie, M. D. Scafetta, E. J. Moon, A. L. Krick, R. J. Sichel-Tissot, and S. J. May, *Appl. Phys. Lett.* **105**, 062110 (2014).
- <sup>33</sup>J. F. Ihlefeld, N. J. Podraza, Z. K. Liu, R. C. Rai, X. Xu, T. Heeg, Y. B. Chen, J. Li, R. W. Collins, J. L. Musfeldt, X. Q. Pan, J. Schubert, R. Ramesh, and D. G. Schlom, *Appl. Phys. Lett.* **92**, 142908 (2008).
- <sup>34</sup>L. Wang, Y. Du, P. V. Sushko, M. E. Bowden, K. A. Stoerzinger, S. M. Heald, M. D. Scafetta, T. C. Kaspar, and S. A. Chambers, *Phys. Rev. Mater.* **3**, 025401 (2019).
- <sup>35</sup>T. Arima, Y. Tokura, and J. B. Torrance, *Phys. Rev. B* **48**, 17006 (1993).
- <sup>36</sup>H. Wadati, D. Kobayashi, H. Kumigashira, K. Okazaki, T. Mizokawa, A. Fujimori, K. Horiba, M. Oshima, N. Hamada, M. Lippmaa, M. Kawasaki, and H. Koinuma, *Phys. Rev. B* **71**, 035108 (2005).
- <sup>37</sup>N. Kovaleva, A. Boris, C. Bernhard, A. Kulakov, A. Pimenov, A. Balbashov, G. Khaliullin, and B. Keimer, *Phys. Rev. Lett.* **93**, 147204 (2004).
- <sup>38</sup>E. Kozik, E. Burovski, V. W. Scarola, and M. Troyer, *Phys. Rev. B* **87**, 205102 (2013).
- <sup>39</sup>A. Khare, D. Shin, T. S. Yoo, M. Kim, T. D. Kang, J. Lee, S. Roh, I.-H. Jung, J. Hwang, S. W. Kim, T. W. Noh, H. Ohta, and W. S. Choi, *Adv. Mater.* **29**, 1606566 (2017).
- <sup>40</sup>J. Hombo, Y. Matsumoto, and T. Kawano, *J. Solid State Chem.* **84**, 138 (1990).
- <sup>41</sup>I. G. Austin and N. F. Mott, *Adv. Phys.* **18**, 41 (1969).
- <sup>42</sup>R. C. Devlin, A. L. Krick, R. J. Sichel-Tissot, Y. J. Xie, and S. J. May, *J. Appl. Phys.* **115**, 233704 (2014).
- <sup>43</sup>H. C. Wang, C. L. Wang, J. L. Zhang, W. B. Su, J. Liu, M. L. Zhao, N. Yin, Y. G. Lv, and L. M. Mei, *Curr. Appl. Phys.* **10**, 866 (2010).
- <sup>44</sup>T. Das, J. D. Nicholas, and Y. Qi, *J. Mater. Chem. A* **5**, 4493 (2017).
- <sup>45</sup>A. Rothschild, W. Menesklou, H. L. Tuller, and E. Ivers-Tiffée, *Chem. Mater.* **18**, 3651 (2006).